New Journal of Physics
The open access journal at the forefront of physics

Deutsche Physikalische Gesellschaft DPG
IOP Institute of Physics

Coupling between rotational and translational motions of a vibrated polygonal disk

To cite this article: Simeon Völkel and Kai Huang 2020 *New J. Phys.* **22** 123018

IOP Publishing New J. Phys. 22 (2020) 123018 https://doi.org/10.1088/1367-2630/abcc9a

New Journal of Physics
The open access journal at the forefront of physics

Deutsche Physikalische Gesellschaft DPG
IOP Institute of Physics
Published in partnership with: Deutsche Physikalische Gesellschaft and the Institute of Physics

OPEN ACCESS

RECEIVED
23 September 2020

REVISED
16 November 2020

ACCEPTED FOR PUBLICATION
20 November 2020

PUBLISHED
21 December 2020

PAPER

Coupling between rotational and translational motions of a vibrated polygonal disk

Simeon Völkel[1],* and Kai Huang[1],[2]

[1] Experimentalphysik V, Universität Bayreuth, 95440 Bayreuth, Germany
[2] Division of Natural and Applied Sciences, Duke Kunshan University, 215306, Kunshan, Jiangsu, People's Republic of China
* Author to whom any correspondence should be addressed.

E-mail: simeon.voelkel@uni-bayreuth.de and kh380@duke.edu

Keywords: nonlinear dynamics, granular materials, granular monolayers, nonequilibrium systems

Abstract

We investigate experimentally the dynamics of a single polygonal disk (regular n-gon with $3 \leqslant n \leqslant 8$) confined in a closed container under vertical vibrations against gravity. The disks tend to precess continuously upon vibrations, transferring mechanical energy into rotational and lateral translational degrees of freedom (DoF). An analysis of the velocity distribution functions in both DoF suggests that the mobility in both DoF are coupled with each other, exhibiting a characteristic angular velocity that depends on confinement and disk shape. The characteristic angular velocity can be captured with an analytical model considering sustainable precession due to continuous driving. Depending on confinement, translational and rotational kinetic energy fluctuations within one vibration cycle can be synchronized with each other and there exists a regime where injected energy is equally distributed in different DoF. Depending on n, the tendency for the disk to precess varies and there exists a regime ($n \leqslant 6$) where persistent rotation of the disk rarely lasts longer than one vibration period. Our results suggest the possibility of tuning energy injection into different DoF in vibrated granular disk mono-layers via shape design and confinement.

1. Introduction

An object driven by mechanical vibrations (e.g., a ball bouncing on a vibrating plate) exhibits rich nonlinear and chaotic dynamics [1]. From spheres to dimers and trimers [2–5], from self-propelled rods and polar disks to 'vibrots' [6–12], from chiral wires to screw nuts and bolt-like particles [13–15], the collective behavior of vibrofluidized particles of various shapes has received a growing interest in the past decades. The dissipative feature characterizes driven granular particles as a model system for a better understanding of widespread nonequilibrium systems in nature, such as the collective dynamics of bacteria colonies, migration of birds, and pedestrian flow [16–18]. Depending on the object shape, driving and confining conditions, the dynamical behavior of a single particle differs, owing to distinct ways of re-distributing the injected kinetic energy into different DoF. Due to continuous in- and out-flux of energy, granular systems are driven far from thermodynamic equilibrium. Although fundamental concepts such as free energy minimization and equipartition cannot be taken as granted in such systems, recent investigations on the collective behavior of vibro-fluidized granular materials reveal the similarity between the stationary states in the nonequilibrium *model* system and the thermally driven atomic and colloidal systems, such as crystallization, surface melting, phase separation, and liquid-crystal mesophase [10, 19–24].

In a recent investigation [14], we showed that a monolayer of hexagonal disks sandwiched between two parallel plates under vertical vibrations against gravity tend to assemble themselves into a state with positional but without orientational order, reminiscent to plastic crystals composed of hard polyhedra (in three dimensions) or polygonal disks (in two dimensions) [25, 26]. As any 'macroscopic' collective behavior arises from the mobility of individual building blocks as well as the interactions between them, we focus here on the dynamics of a single polygonal disk under vertical vibrations. In particular, we investigate how a change of particle shape and confinement influences its motion in both translational and rotational degrees of freedom as well as the coupling in between.

2. Methods

Side and top views of the experimental setup are sketched in figures 1(a) and (b) respectively. N regular n-gon disks ($3 \leqslant n \leqslant 8$ as shown in figure 1(d)) of incircle diameter D and height h are confined to a cylindrical container of height H and diameter $2R$. The horizontally aligned container is observed from above and vibrated against gravity g. It is driven sinusoidally using an electromagnetic vibrator (Tira TV50350). The dimensionless acceleration $\Gamma = (2\pi f)^2 z_0/g$ with frequency f and amplitude z_0 is controlled via a function generator (Agilent FG33220) and an accelerometer (Dytran 3035B2). The bottom and lid of the container are made from 1 cm thick polycarbonate (Bayer Makrolon) to provide uniform driving. The disks are cut from brass (CuZn39Pb5, density $\varrho = 8.5$ g cm^{-3}) and have a central circular hole of diameter d, to facilitate fast and precise detection of particle location even in the case of close packing. The triggering of the camera (Lumenera Lt425M and IDT MotionScope M3) is synchronized to the driving, as is the stroboscopic LED background illumination used to achieve high contrast (see [10, 27] for additional details).

The captured raw images are subjected to image analysis. Figure 1(c) shows a sample image after background removal with particle position and orientation marked. The image analysis procedure is split in two steps, finding the particle center (x- and y-coordinate) followed by determining its orientation Ψ. For the rest of this investigation we focus on single particle dynamics. Therefore we place in the container only a single disk ($N = 1$) or very few disks ($N = 8$ to 16) sufficiently apart from each other to avoid interactions, confine them horizontally to the field of view of the camera (5 cm × 5 cm) using black electrostatic discharge foam and make sure there is no influence from the boundary.

For finding the particle center, the rotational symmetry of the central drilling is exploited. For particles lying flat on the imaging plane, finding their centers translates to finding the centers of circles with diameter d in the image. While agitated, the particles can tilt slightly. In the background-illuminated image the hole's edges become two ellipse arcs, which are slightly shifted towards each other. As the particles have a finite height h, the vertical confinement H limits the maximum tilting angle, e.g. for a disk of circular or n-gon shape with even n, to

$$\theta_{\max} = 2 \cdot \ \arctan\left[\left(D - \sqrt{D^2 + h^2 - H^2}\right)/(h + H)\right]. \tag{1}$$

Consequently, the maximum distortion from a circle (in radial direction) is within 7% of its radius in the worst case of the experiments presented here and can be ignored. Finding the centers of circles can be achieved efficiently using the circle Hough transformation [28–30]. The required processing time can become independent of the input image complexity (e.g., number of particle edge pixels) if convolutional approaches are used [31].

The Canny edge filter [32] is used to detect particle contours. As it is a non-linear edge filter, it can not be combined with the radius search to a single convolution kernel as proposed in [31]. However, the advantage of the Canny edge filter is that it avoids cancellation of votes in the Hough accumulator[3], and thus enables accurate measurement of disk position with subpixel resolution.

The binary edge image is subsequently convolved with a truncated Hough cone consisting of blurred circles of different radii $\tilde{r}$ close to the expected value of $d/2$. In polar coordinates (r, φ), the density of Hough votes can be written as $W \cdot \frac{1}{r} \cdot \exp\left(-\frac{(r-\tilde{r})^2}{2\,\sigma^2}\right)$, where $\sigma = 0.5\text{px}$ sets the amount of blurring to accomodate discrete sampling and $W = 3/[2 + \max(d/2 - 1\text{px}, \tilde{r})/\tilde{r}]$ is an empirical prefactor as a penalty to circles smaller than the expected ones.

The Hough accumulator resulting from the convolution is then searched for the N highest isolated peaks, where N is the known number of particles to be found. To speed up this search, values smaller than a dynamically adjusted limit are thresholded to zero, making the Hough accumulator sparse. After sorting, it is traversed descendingly and the locations of the N highest *isolated* peaks are found. The first entry of the sorted list (a global maximum) is called *isolated* by definition. Subsequently peaks are isolated by ignoring Hough space entries within a threshold distance r_{p} to *isolated* peaks, until N center locations are found.

As the last step of locating the particles, subpixel refinement is performed for each identified particle position. The subpixel shift Δ of the peak location along the x-, y- and r-axis of the Hough accumulator is estimated with $\Delta = 0.5\ \text{px} - \tilde{\sigma}^2/1\ \text{px} \cdot \ln(p/q)$, where p is the value of an isolated peak and q its highest

---

[3] Note that cancellation of votes in the Hough accumulator is a problem inherent to all linear edge filters, making *accurate* parameter estimation infeasible.

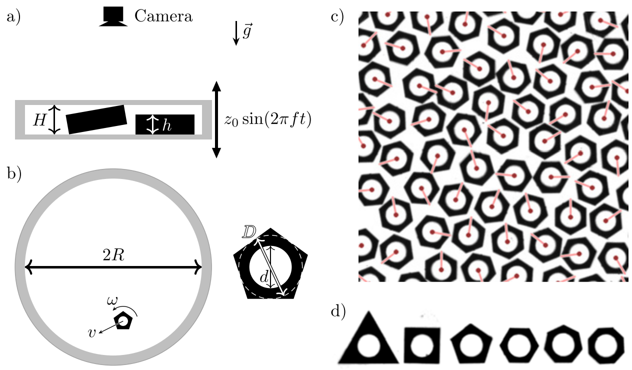

Figure 1. (a) Sketch of the set-up with various definitions (see text for details) in side and (b) top view. (c) Zoom-in view of an image after background removal with markers showing the position and orientation of individual disks, obtained with image analysis. (d) n-polygon particles with $3 \leqslant n \leqslant 8$ but the same incircle diameter $D = 6$ mm and height $h = 2$ mm.

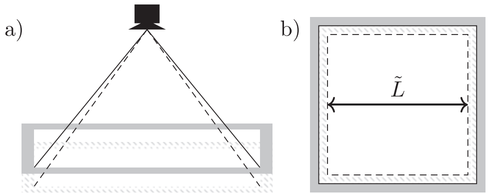

Figure 2. Determination of the vertical position of the container using a top view camera.

neighbor along the corresponding axis. The shape of the peak is assumed to be a Gaussian of width $\tilde{\sigma} = 2\sigma$ for x and y and $\tilde{\sigma} = 2\sqrt{2}\sigma$ for r respectively.

For determining the orientation of each particle, a Fourier analysis of its outer contour is performed. Here, the longest contour C of the binary edge image within a circular mask of inner radius r_i and outer radius r_o (with the particle center as origin) is transformed to polar coordinates (r, φ). $C(r, \varphi)$ is approximated using the 0th, 1st, 2nd and nth Fourier mode, corresponding to the mean radius of the contour, a shift of the detected center with respect to the outer contour, a tilting of the particle, and the corners or the particle respectively. The phase angle of the nth Fourier mode of $C(r, \varphi)$ indicates (modulo $2\pi/n$) the desired orientation Ψ of the regular n-gon.

As sketched in figure 2(a), the viewing angle of the container bottom varies with its vertical position. Stepping further than a previous investigation [33], we obtain the third-dimensional information quantitatively from the top view images. The apparent length $\tilde{L}$ in the top view image figure 2(b) changes slightly when using a conventional entocentric lens. By tracing the positions of two fixed segments of the container wall with subpixel resolution, we obtain the relative vertical position of the container, which is subsequently scaled to an absolute vertical displacement using the accelerometer reading. As illustrated below in section 5, a spatial resolution down to a few hundredths of a pixel can be achieved.

Finally, the particle motion is traced based on the image analysis results, assuming every particle moves to the closest position of a particle in the next frame. This assumption is checked for plausibility by verifying that the mapping between particles in two consequent frames is always bijective. After identifying the same particle in consequent frames, its orientation is traced, assuming that the sampling rate fulfills the Nyquist criterion. This assumption is reasonable as the change of orientation between two consequent frames is typically more than an order of magnitude smaller than $2\pi/n$.

3. Coupling between translational and rotational motion

Based on the tracing results, the average velocity between two consecutive frames is obtained. Figure 3 shows scatter plots of angular ω vs translational v velocities of the particle center for $n = 6$ and 5. These plots are representative for all results obtained with an even or odd number of corners explored here. For polygonal particles with even n, three clusters of points (cf figure 3(a)) whereas for odd n only two distinct clusters are found (cf figure 3(b)). We note that in both cases the position, shape and density of the clusters are symmetric with respect to zero on the ω axis. This suggests that the rotation mechanism has no

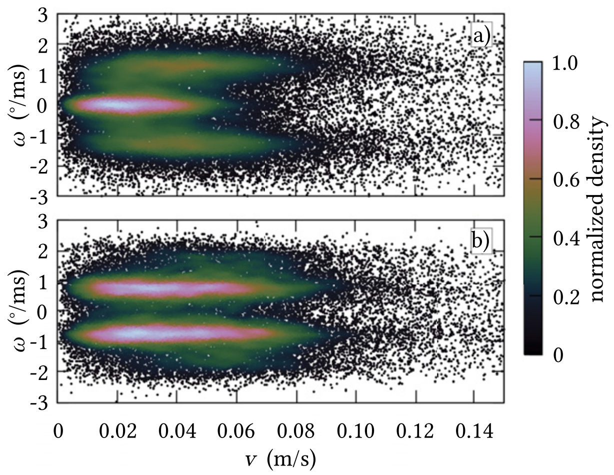

Figure 3. Scatter plot of the angular velocity ω with respect to the particle's center vs its horizontal velocity v obtained from consequent top view images sampled at a rate of 1000 Hz over 45 s for a single (a) hexagonal ($n = 6$, $N = 10$) and (b) pentagonal ($n = 5$, $N = 12$) disk. Parameters: $f = 50$ Hz, $\Gamma = 7$, $H = 3.9$ mm, $h = 2$ mm, $D = 6$ mm. The color code corresponds to the local area density of data-points obtained with a Gaussian kernel density estimator using the bandwidths 2.9 mm s^{-1} and 0.073° m s^{-1} in (a) and 2.4 mm s^{-1} and 0.06° m s^{-1} in (b).

preferential direction so that clockwise and counterclockwise rotation have equal likelihood. For even n (cf figure 3(a)), the central cluster around $\omega = 0$ is typically very prominent and represents a clapping motion (clattering mode) of the disk [34]. For off-centered clusters, the typical translational velocity lies significantly higher than for the clapping motion. This suggests that disks in different rotational modes, i.e. clattering or precessing, tends to have different v, indicating a coupling between rotational and translational DoF. For odd n (cf figure 3(b)), only the two off-centered clusters are found, meaning that polygons with odd n have a significantly higher tendency to precess than with even n. This can be easily understood, as for odd n each side of the polygon faces a corner on the opposite side, so that small perturbations due to roughness quickly make the clapping motion unstable.

The position of the clusters changes with the confinement and particle shape. The translational velocity distribution is investigated in detail in appendix A where we show that at timescales longer than half a vibration period the particle effectively diffuses in the lateral direction. In the following section we concentrate on the rotational motion for a quantitative analysis.

4. Characteristic angular velocities

Figure 4 shows the probability density P_ω of the angular velocity ω for the same parameters as in figure 3. For the hexagonal disk (cf figure 4(a)) the distribution shows three peaks and can be described fairly well by a sum of three Gaussian distributions $\mathcal{N}$ symmetrically arranged around $\omega = 0$:

$$\omega \sim \sum_{k=-1}^{1} \mathcal{N}(k\,\omega_\mathrm{r}, \sigma_k) \cdot p_k, \tag{2}$$

where ω_r is the characteristic angular velocity to be obtained. During fitting we fix $\sigma_{-1} = \sigma_{+1}$ as the variations in ω do not appear to depend on its sign. We allow $p_{-1} \neq p_{+1}$ due to the finite observation period. For the central peak around $\omega = 0$ only the standard deviation σ_0 is fitted as $p_0 = 1 - p_{-1} - p_{+1}$ is fixed due to the normalization of P_ω. By fitting the remaining five free parameters (ω_r, σ_0, σ_{+1}, p_{-1}, p_{+1}), the characteristic angular velocity ω_r is determined. Its dependence on the confinement is discussed below.

In the case of the pentagonal disk (cf figure 4(b)), two additional Gaussians around $\pm 2\omega_\mathrm{r}$ have to be added for a reasonable fit:

$$\omega \sim \sum_{k=-2}^{2} \mathcal{N}(k\,\omega_\mathrm{r}, \sigma_k) \cdot p_k. \tag{3}$$

Remarkably, we find that the peaks at $2\omega_\mathrm{r}$ have in good approximation the doubled width of the inner ones and appear to have the same relative probabilities. By exploiting this observation, we reduce the number of degrees of freedom without decreasing the quality of the fit visibly. More precisely, by fixing $p_{+2}/p_{-2} = p_{+1}/p_{-1}$ and prescribing $\sigma_{+2} = \sigma_{-2} = 2\sigma_{+1} = 2\sigma_{-1}$ only a single additional degree of freedom, p_{+2}, is added. The presence of two peaks per side suggests that there exist different ways of injecting energy

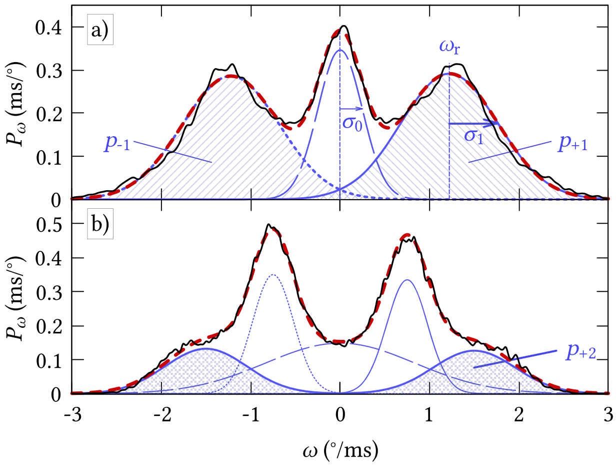

Figure 4. Kernel density estimate (black solid line) for the probability density P_ω of the angular velocity ω of the (a) hexagonal and (b) pentagonal disk shown in figure 3. Fit (red dashed line) with a summation of three (a) and five (b) symmetrically arranged normal distributions (see equation (2) and equation (3) for more details). Parameters used for fitting are sketched in blue. The Gaussian kernel's bandwidth is chosen optimally using the improved Sheather-Jones algorithm [35] to 0.030° m s^{-1} and 0.019° m s^{-1} respectively.

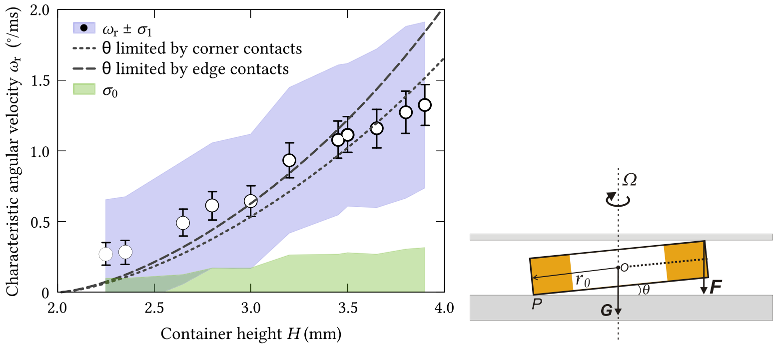

Figure 5. Left: dependency of a hexagonal particle's characteristic angular velocity ω_r on the vertical confinement H, compared to equation (5) with different restrictions for θ. $N = 1$, other experimental parameters are the same as in figure 3(a). Shaded regions indicate the standard deviation σ_i of the corresponding normal distributions of ω shown in figure 4(a) for rotating (blue) and clapping (green) motion. The uncertainty of ω_r is estimated from σ_1 assuming independent measurements after 100 vibration cycles. The ratio of the inner and outer radius of the data points, indicated by the thickness of the data points, corresponds to the probability for the particle to be classified as precessing according to the fit illustrated in figure 4. Right: side view of a polygonal disk with various definitions.

into the rotational DoF. Note that the second peak arises not only for disks with odd number of edges as it is also observed for $n = 4$. In general this feature appears to be more prominent for lower n. For instance, the ratio p_{+2}/p_{+1} for $n = 6$ is an order of magnitude smaller than in the case of $n = 5$.

Based on ω_r obtained in figure 4(a), we explore systematically the influence of confinement H on particle mobility. As shown in figure 5, the angular velocity increases monotonically with H. This is in agreement with a model considering that rotation arises predominately from the precession of the disk ([14], and references therein).

More specifically, the model considers a circular disk (i.e., the case of $n \to \infty$) with a radius of r_0 and height h. Similar to a coin spinning on a rigid surface, there exists a coupling between precession and rotation for the case of rolling without sliding. As the contact point of the disk draws a circle of radius $r_c < r_0$, the disk rolls actually over a distance larger than $2\pi r_c$ during one precession period $1/\Omega$. With a certain confinement H, the maximum tilting angle is limited by $\theta_{\max}$ of equation (1) with $D = 2r_0$. The model assumes $\theta = \theta_{\max}$ and therefore the angular velocity varies with confinement H. In addition to the influence of gravity, as considered in existing literature, see e.g. [36–38], here the additional influence from the vibrating plate (e.g., torque induced by the force F for the case of colliding with the container lid) has to be considered. Consequently, the precession rate can be estimated with [14]:

$$\Omega = \sqrt{\frac{G r_0 (1 + 2\Gamma)}{I_{r,P}\ \sin\ \theta}}, \qquad (4)$$

where G is the gravity of the disk, Γ is the maximum dimensionless acceleration and $I_{\mathrm{r,P}}$ is the moment of inertia along the radial direction passing through contact point P. Here, the value for a regular n-gon disk is used, $I_{\mathrm{r,P}} = \varrho h \left[\frac{n}{64}D^4\left(\cos\frac{\pi}{n}\right)^{-2}\left(1-\frac{2}{3}\sin^2\frac{\pi}{n}\right)\ \tan\frac{\pi}{n} - \frac{\pi}{64}d^4 + \frac{h^2}{12}\left(nD^2\ \tan\frac{\pi}{n} - \pi d^2\right)\right]$. It is calculated by considering n isosceles triangles, subtracting the circular hole, taking advantage of the perpendicular axis theorem and using the parallel axis theorem when integrating along the third dimension [39]. To match the experimental conditions, we use the parameters for the hexagonal disk ($n = 6$, $h = 2$ mm, $D = 6$ mm, $d = 2$ mm) to estimate the characteristic rotation speed of the disk viewed from top using

$$\omega_{\mathrm{r}} = (1/\cos\ \theta - 1)\Omega\,. \tag{5}$$

Figure 5 compares the experimental data to this precession model using the largest value of θ compatible with corner contacts (dotted line) and edge contacts (dashed line) at bottom and lid.

In reality, the rolling motion of the disk is always accompanied with energy dissipation arising from air drag, sliding, rolling friction, etc. The frequent collisions between the disk and the vibrating plates also lead to frequent detachment between the disk and the container. Although the simplified model does not consider the details described above, it provides nevertheless a reasonable estimation of the characteristic angular velocity ω_{r} and its dependence on H without any fit parameters, as shown in figure 5.

The fraction of time spent by the particle in different modes of motion is captured by the coefficients p_k in equations (2) and (3). The hexagonal particle is classified as precessing 98 [4] to 72 percent of the time as H grows (see figure 5). For $H < 2.8$ mm the shaded areas indicate that σ_0 and σ_1 overlap at least partially. This could give a hint why ω_{r} seems to be systematically overestimated for low confinement heights compared to the model: as ω_{r} is extracted from 'shoulders' of a central clattering mode, a lower signal-to-noise ratio has to be expected here than for high H where the modes are clearly separable.

5. Energy fluctuations within one vibration cycle

In order to investigate the dynamics within one vibration period $T_0 = f^{-1}$ we average the kinetic energy at fixed phase over more than 2200 vibration periods, which is shown in figure 6. Note that a sufficient sampling rate is needed for the following analysis, as the translational velocity distribution can be qualitatively different if the sampling rate is reduced, as shown in appendix A.

The upper panel of figure 6 compares the vertical position of the container during one vibration cycle to the induced sinusoidal vibration and shows an excellent agreement for all H. Even though the apparent container size varies only by less than 1.2px, the total harmonic distortion of the signal as defined in [40] is $\mathrm{THD_R} = 4(2)\%$.

The lower panel of figure 6 shows the fluctuations of the kinetic energy of a hexagonal disk within one vibration period for different vertical confinement H. Here, only the lateral movement and rotation in the container plane (as detected by the top view camera) are considered. The squares and filled circles break down the translational and rotational contributions to the kinetic energy, $E_{\mathrm{kin,lat}} = m\,v^2/2$ and $E_{\mathrm{kin,rot}} = I_n\omega^2/2$ respectively, where $I_n = \varrho h\left[\frac{n}{32}D^4\ \tan\frac{\pi}{n}\left(\cos\frac{\pi}{n}\right)^{-2}\left(1-\frac{2}{3}\sin^2\frac{\pi}{n}\right) - \frac{\pi}{32}d^4\right]$ denotes the moment of inertia of the $n-$gon particle with respect to its symmetry axis. The thickness of the solid lines indicates the respective standard error assuming statistical independence of the consecutive vibration periods used for averaging, which is justified according to the following analysis in section 6.

For all confinement heights H, $E_{\mathrm{kin,rot}}$ shows two peaks per vibration period, suggesting that both collisions with the lid and with the container bottom lead to a similar kinetic energy injection into the rotational DoF. The average value of $E_{\mathrm{kin,rot}}$ rises continuously with increasing H in agreement with the growth of ω_{r} predicted by the model, although the probability for the disk to precess decreases as H grows (see the change of data point thickness in figure 5).

In contrast, the lateral translational kinetic energy $E_{\mathrm{kin,lat}}$ shows a qualitatively different behavior: The peak in the second half of a vibration period is clearly suppressed as H decreases. In the case of $H < 3.2$ mm, only one peak can be clearly distinguished. This qualitative difference arises presumably from the way of energy injection: Torque induced precession always leads to rotation upon collisions with the container, while force applied vertically on the tips or edges of the disk will not necessarily lead to translational motion in the horizontal direction.

Remarkably, as H decreases, there is a tendency for $E_{\mathrm{kin,lat}}$ and $E_{\mathrm{kin,rot}}$ in the observed DoF (i. e., two translational DoF perpendicular to $\boldsymbol{g}$ and one rotational DoF around $\boldsymbol{g}$) to overlap with each other in the

---

[4] This corresponds to the two lowest confinement heights where the standard deviations of the clockwise and the counterclockwise precession mode overlap each other significantly, impacting the reliability of the classification.

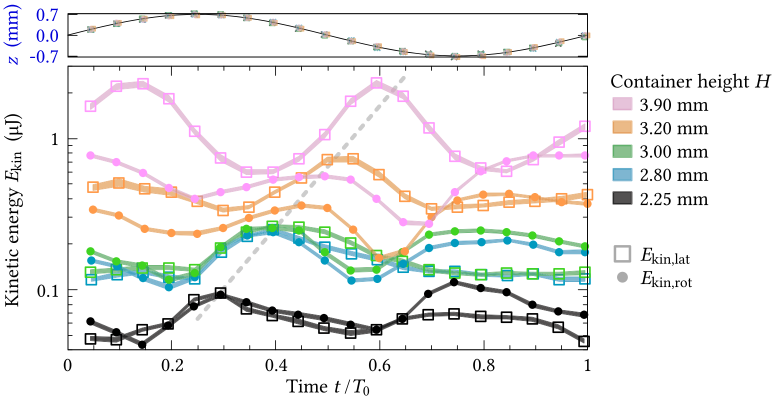

Figure 6. Top: vertical position z of the container within one vibration cycle obtained from top view images. Bottom: average lateral translational $E_{\mathrm{kin,lat}}$ (☐) and rotational kinetic energy $E_{\mathrm{kin,rot}}$ (●) of the hexagonal disk of figure 5 within one vibration cycle for various confinement H. The gray dashed line is a guide to the eyes highlighting the phase-shift of the maximum kinetic energy.

first half of the vibration cycle. Note that this is different from a previous observation of vibrofluidized granular rods under microgravity condition [41], where the kinetic energy in one translational DoF and two observed rotational DoF was found to be equal with each other. The mechanism behind such apparent 'equipartition' deserves further investigation in the future as it helps constructing nonequilibrium model systems with granular particles. However, we find $E_{\mathrm{kin,lat}} < E_{\mathrm{kin,rot}}$ in the second vibration half period. Furthermore, these differences within one vibration period apparently disappear abruptly for larger H. For $H \geqslant 3.2$ mm, $E_{\mathrm{kin,lat}}$ exceeds $E_{\mathrm{kin,rot}}$ by more than a factor of two on average. Note that the relative amount of energy injection into the different DoF changes with H, as the vertical confinement drives rotation arising from precession and yet tends to hinder a horizontal translation of the vibrated particle.

Finally, the phase-shift of the maximum for each kinetic energy contribution when changing H constitutes another prominent feature in figure 6, as highlighted by the gray dashed line. With increasing H the maxima shift to later times. This trend is expected as the traveling distance of a disk from container bottom to the lid (and vice versa) increases. The phase-shift applies to both rotational and translational DoF, as they are coupled with each other. For small H, the first peak for the kinetic energy of either translational or rotational DoF overlaps with each other. For $H \geqslant 3.2$ mm, the peak of $E_{\mathrm{kin,lat}}$ lags slightly behind $E_{\mathrm{kin,rot}}$. Such a difference suggests that the coupling between different DoF as well as the distribution of energy injection can be tuned by confinement. This abrupt phase-shift tuned by H and the related transition between different coupling modes is further illustrated by means of the cross-correlation function in appendix B.

In short, the above analysis suggests that confinement plays an essential role in determining the distribution of energy injection in different DoF as well as coupling in between.

6. Shape tuned 'memory' effect

Finally, we address the influence of n on the 'memory' of the system, which is characterized by the autocorrelation function. After collision, the disk tends to keep its motion, i.e., retains a certain level of 'memory', while frequent collisions with the container lead to the loss of 'memory'. Using autocorrelation functions of the disk motion in both DoF, we analyze the influence of particle shape on this effect.

Figure 7 compares the autocorrelations $r_{v,v}$, $r_{\omega,\omega}$ and $r_{|\omega|,|\omega|}$ of the lateral velocity v, the angular velocity ω and its absolute value $|\omega|$ respectively for two different container heights H in the case of a pentagonal disk. In alignment with the periodicity of lateral velocity shown in figure 6 for a hexagonal disk, $r_{v,v}$ peaks at multiples of T_0 and $T_0/2$ for the case of $H = 3$ mm and 3.9 mm, respectively, suggesting the influence of collisions with container bottom and lid. For low H, the autocorrelation of the absolute angular velocity $r_{|\omega|,|\omega|}$ also oscillates around zero, showing clearly a periodic behavior. This is not surprising as both DoF are coupled with each other. As H increases, the magnitude of the peaks for $r_{v,v}$ drop dramatically, suggesting a stronger influence from the randomness due to strong impacts with the container. Note that different H leads to different modes. For the signed value of the angular velocity (instead of its absolute value), the autocorrelation function shows a clearly different trend. No clear periodicity can be found and $r_{\omega,\omega}$ decays exponentially, as shown in the insets of figure 7.

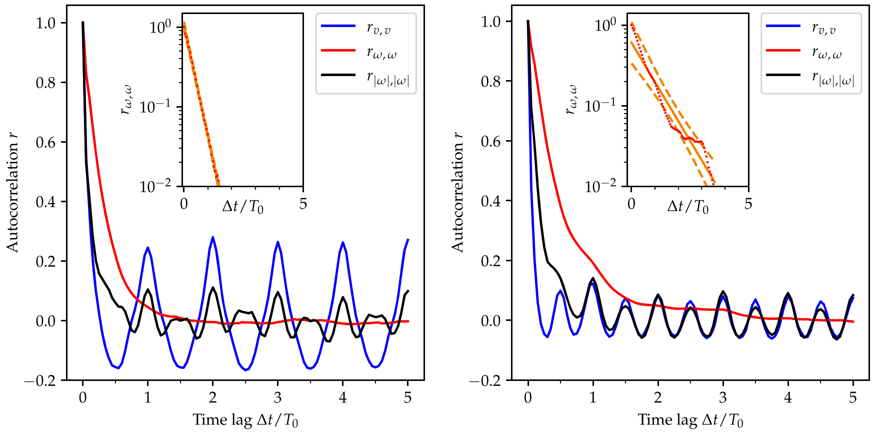

Figure 7. Normalized autocorrelation of velocity v (blue), angular velocity ω (red) and its absolute value $|\omega|$ (black) of a pentagonal disk ($n = 5$) for $H = 3$ mm (left) and $H = 3.9$ mm (right). Other experimental parameters are the same as in figure 3(b). The insets highlight the exponential decay of the autocorrelation function of ω. The decay time is extracted by fitting a straight line (orange), the dashed lines indicate the uncertainty.

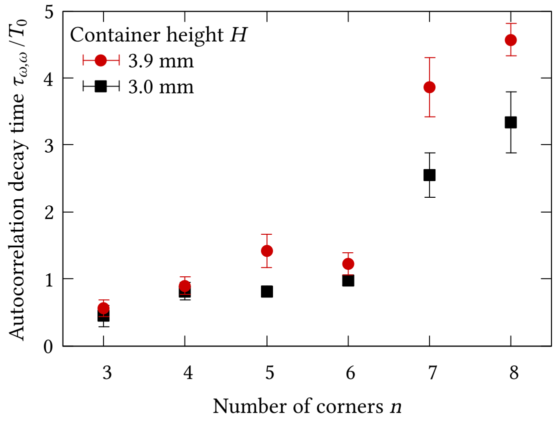

Figure 8. Decay time of the angular velocity autocorrelation function at various n for two container heights. $N = 8, 12, 12, 10, 16, 16$ for $n = 3, 4, 5, 6, 7, 8$ respectively. Other parameters are the same as in figure 7.

As shown in figure 4, the disk may rotate in either direction with the same probability. Qualitatively speaking, the change of r due to $|.|$ suggests a frequent change of rotations due to collision. The periodicity of driving becomes visible when considering the kinetic energy scale or absolute value of the angular velocity. The fact that $r_{\omega,\omega}$ does not show a clearly periodic behavior suggests that change of rotation speed (i.e., torque applied while colliding) itself tends to persist after collision. This provides an opportunity for us to quantitatively investigate the 'memory' carried by the agitated disk through the characteristic decay time $\tau_{\omega,\omega}$, which is defined as the time scale for $r_{\omega,\omega}$ to decay from 1 to e^{-1}.

Figure 8 plots the decay time for various n and two different H. In comparison to confinement, the number of corners has the more dramatic effect on the 'memory' of the disk: the closer the disk shape is to a circle, the longer the autocorrelation decay time. Qualitatively, this can be understood as the chance for a disk to keep its rotation increases as n increases, as the corresponding potential energy barrier is smaller. Quantitatively, the decay time tends to stay within one vibration period for $n \leqslant 6$, meaning that the 'memory' is lost after each vibration cycle, and the influence from H is weak. This suggests that samples collected at a rate lower than the driving frequency can be considered independent of each other. As $n = 7$ or higher (the disk shape getting closer to a circle), the decay time grows monotonically and the influence from H becomes prominent, suggesting a higher probability for persistent rotation.

7. Conclusions and outlook

To summarize, we characterize systematically the influence of confinement (i.e., height of the container) and shape on the motion of a single regular n-gon disk in both translational and rotational degrees of freedom under vibrations. Generally speaking, a vibrated polygonal disk tends to rotate due to precession induced by gravity as well as collisions with the container and the rotation speed is tuned by the confinement height H. For a disk with even number of edges, there exists an additional clattering mode with zero angular velocity.

By means of circular Hough transformation and Fourier analysis of the contour, we analyze the coupling between rotational and translational degrees of freedom of the polygonal disk quantitatively and find that the probability for a disk to rotate can be decomposed into symmetrically arranged normal distributions peaked at a characteristic angular velocity.

In order to explore particle motion within one vibration cycle, we develop an algorithm that can successfully obtain the container position from tiny changes (1.2 pixel) of the container's width upon vibration along the viewing direction. Consequent analysis on the kinetic energy fluctuations within one vibration period shows a clear dependence on the confinement and a tendency of equal energy distribution in both observable DoF at small confinement.

The time scale associated with the dynamics of the disks is characterized by means of the autocorrelation function. We find that the decay time of $r_{\omega,\omega}$ increases monotonically with n. The fact that it becomes smaller than the vibration period for $n \leqslant 6$ indicates the loss of 'memory' in rotational DoF and consequently velocities sampled once per vibration period can be considered as independent of each other.

In the future, a more quantitative understanding of the critical confinement and influence of edge number is needed, as the two control parameters provide a pathway to design preferred trajectories of individual polygonal disks as well as the kinetic energy input into different DoF. Note that an assembly of granular 'walkers' with equipartition of energy injection could serve as a perfect model system for extending statistical mechanics tools to investigate widespread active matter.

Acknowledgments

We are grateful to Manuel Baur for his preliminary work on the experimental setup and to Klaus Ötter for technical support. Inspiring discussions with Ingo Rehberg and Valentin Dichtl are gratefully acknowledged. This work is supported by the Deutsche Forschungsgemeinschaft through Grant no HU1939/4-1. This publication was funded by the German Research Foundation (DFG) and the University of Bayreuth in the funding programme Open Access Publishing.

Appendix A. Translational velocity distribution

Figure A1 shows a comparison of the lateral velocity distribution obtained with different sampling rates; twice (black) or 20 times (red) per vibration period (the same as in figure 3).

The outer panels display the distributions as probability densities P_v, estimated using a Gaussian kernel density estimator of variable bandwith [42]. The limited support due to $v > 0$ is accounted for using the reflection method [43]. The hyperparameter is optimized using leave-one-out maximum-likelihood cross-validation [44, 45]. The shift towards lower velocities for the lower sampling rate is very prominent. When sampling ten times as often, the mean of the distribution differs by a factor of 2.2 for both the hexagonal (figure A1(a)) and the pentagonal (figure A1(b)) disk. The lower mean for rarer sampling confirms that the disks change the direction of their translational motion within the timeframe of half a vibration period.

The insets show the corresponding cumulative distribution function $F(x) = \int_{-\infty}^{x} P(x')\mathrm{d}x'$ to avoid any visualization parameters. Here, the tail of the distribution is highlighted by plotting the empirical complementary cumulative distribution function $1 - F_{v^2}$ on a logarithmic axis. As the black curve is close to a straight line, the coarser sampled lateral velocity distribution is close to the Maxwell–Boltzmann distribution in two dimensions. The particle thus effectively diffuses in the lateral direction at long timescales. This is reminiscent of the rotational random walk found in [14] and raises the question to which extend random motion in the rotational and translational DoF are coupled. The velocity fluctuations within one vibration cycle are discussed in more detail in section 5.

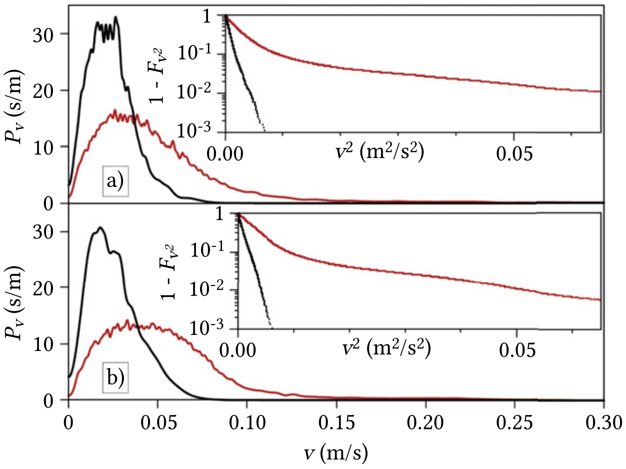

Figure A1. Horizontal velocity distribution for the (a) hexagonal and (b) pentagonal disk when sampling the particle position 20 times per vibration cycle (red), or two times per vibration cycle (black). Other parameters are the same as in figure 3. Note that sampling 20 times per vibration cycle corresponds to 1000 Hz as previously. Outer panels: probability density P_v estimated using the optimal Gaussian kernel density estimator of variable bandwith (see text for details). Insets: complementary cumulative distribution function of the squared velocity.

Appendix B. Confinement controlled coupling

The coupling between translational and rotational DoF is characterized using the zero mean normalized cross-correlation of v^2 and ω^2, shown in figure B1 for different H with the time lag Δt in units of T_0. For better visibility of the underlying structure, bilinear interpolation is used between the sampling points.

For all container heights H, the cross-correlation peaks at zero time lag and shows a regular pattern otherwise. The global maximum at $\Delta t = 0$ indicates an overall in phase coupling between rotation and translation. However, as all aperiodic contributions accumulate in this central peak (similarly to the noise-polluted zero time lag peak in autocorrelations), the periodic response of the system should be instead inferred from the off-center maxima. Their distance of $T_0/2$ indicates collisions with both lid and bottom in a similar manner (for at least one of v or ω), as also indicated in figure 6. For $H < 3.0$ mm, the off-center maxima occur at integer multiples of $T_0/2$, indicating zero phase-shift between rotation and translation for the periodic response of the system, which we call synchronous mode. For $H > 3.0$ mm, the off-center maxima are shifted. Here, rotation precedes the translation by roughly $T_0/8$, giving rise to the asynchronous mode. Taking into account that, according to figure 6, v^2 and ω^2 peak twice per vibration period T_0 we observe a phase-shift close to $90°$ between the two contributions to the total kinetic energy here.

For the case of rolling without sliding, rotation of an Euler's disk is expected to be coupled to the center of mass movement and consequently the kinetic energy in the translational DoF. This expectation is compatible with our observations for small container heights. At $H \approx 3.0$ mm however, the coupling between rotation and translation changes fundamentally, leading to the transition into the asynchronous mode. Note that the phase lag between v^2 and ω^2 as a function of H exhibits a stepwise dependence, reminiscent of the scenario of forced oscillation with a driving dependent phase-shift.

The characterization of the cross-correlation function r_{v^2,ω^2} indicates that, depending on confinement, there exists an abrupt transition from the 'synchronous' mode where the energy peaks of the translational and rotational motion are at the same phase to the 'asynchronous' mode where a phase-shift between different DoF arises.

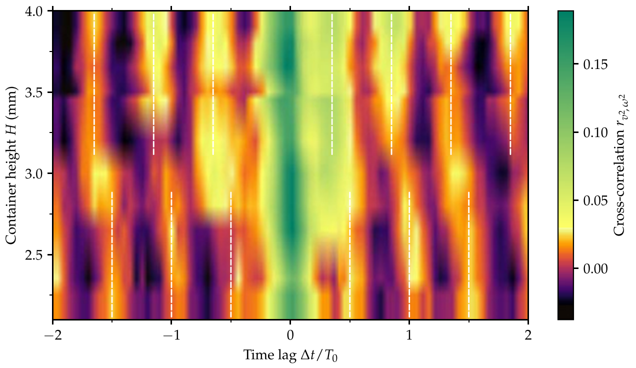

Figure B1. Normalized cross-correlation of lateral translational and rotational contributions to the kinetic energy for the same experimental parameters as in figure 5. The white dashed lines are guides to the eyes highlighting the location of off-center maxima of the cross-correlation for low and high container heights H.

ORCID iDs

Simeon Völkel https://orcid.org/0000-0002-0036-0394
Kai Huang https://orcid.org/0000-0003-0652-713X

References

[1] Tufillaro N and Abbott T 1992 *An Experimental Approach to Nonlinear Dynamics and Chaos* (Reading MA: Addison-Wesley)
[2] Tufillaro N B and Albano A M 1986 Chaotic dynamics of a bouncing ball *Am. J. Phys.* **54** 939–44
[3] Dorbolo S, Volfson D, Tsimring L and Kudrolli A 2005 Dynamics of a bouncing dimer *Phys. Rev. Lett.* **95** 044101
[4] Dorbolo S, Ludewig F and Vandewalle N 2009 Bouncing trimer: a random self-propelled particle, chaos and periodical motions *New J. Phys.* **11** 033016
[5] Wang J, Liu C, Jia Y B and Ma D 2014 Ratchet rotation of a 3D dimer on a vibrating plate *Eur. Phys. J.* E **37** 1
[6] Kudrolli A, Lumay G, Volfson D and Tsimring L S 2008 Swarming and swirling in self-propelled polar granular rods *Phys. Rev. Lett.* **100** 058001
[7] Deseigne J, Dauchot O and Chaté H 2010 Collective motion of vibrated polar disks *Phys. Rev. Lett.* **105** 098001
[8] Yadav V, Chastaing J Y and Kudrolli A 2013 Effect of aspect ratio on the development of order in vibrated granular rods *Phys. Rev.* E **88** 052203
[9] Altshuler E, Pastor J M, Garcimartín A, Zuriguel I and Maza D 2013 Vibrot, a simple device for the conversion of vibration into rotation mediated by friction: preliminary evaluation *PLoS One* **8** e67838
[10] Müller T, de las Heras D, Rehberg I and Huang K 2015 Ordering in granular-rod monolayers driven far from thermodynamic equilibrium *Phys. Rev.* E **91** 062207
[11] Walsh L and Menon N 2016 Ordering and dynamics of vibrated hard squares *J. Stat. Mech.* **2016** 083302
[12] Scholz C, D'Silva S and Pöschel T 2016 Ratcheting and tumbling motion of vibrots *New J. Phys.* **18** 123001
[13] Tsai J C, Ye F, Rodriguez J, Gollub J P and Lubensky T C 2005 A chiral granular gas *Phys. Rev. Lett.* **94** 214301
[14] Baur M and Huang K 2017 Dynamics of wet granular hexagons *Phys. Rev.* E **95** 030901
[15] Takatori S, Baba H, Ichino T, Shew C Y and Yoshikawa K 2018 Cooperative standing-horizontal-standing reentrant transition for numerous solid particles under external vibration *Sci. Rep.* **8** 437
[16] Ramaswamy S 2010 The mechanics and statistics of active matter *Annu. Rev. Condens. Matter Phys.* **1** 323–45
[17] Vicsek T and Zafeiris A 2012 Collective motion *Phys. Rep.* **517** 71–140
[18] Marchetti M C, Joanny J F, Ramaswamy S, Liverpool T B, Prost J, Rao M and Simha R A 2013 Hydrodynamics of soft active matter *Rev. Mod. Phys.* **85** 1143–89
[19] Olafsen J S and Urbach J S 2005 Two-dimensional melting far from equilibrium in a granular monolayer *Phys. Rev. Lett.* **95** 098002
[20] Reis P M, Ingale R A and Shattuck M D 2006 Crystallization of a quasi-two-dimensional granular fluid *Phys. Rev. Lett.* **96** 258001
[21] Eshuis P, van der Weele K, van der Meer D, Bos R and Lohse D 2007 Phase diagram of vertically shaken granular matter *Phys. Fluids* **19** 123301
[22] Huang K, Roeller K and Herminghaus S 2009 Universal and non-universal aspects of wet granular matter under vertical vibrations *Eur. Phys. J. Spec. Top.* **179** 25–32
[23] May C, Wild M, Rehberg I and Huang K 2013 Analog of surface melting in a macroscopic nonequilibrium system *Phys. Rev.* E **88** 062201
[24] Huang K 2015 1/*f* noise on the brink of wet granular melting *New J. Phys.* **17** 083055
[25] Damasceno P F, Engel M and Glotzer S C 2012 Predictive self-assembly of polyhedra into complex structures *Science* **337** 453–7
[26] Anderson J A, Antonaglia J, Millan J A, Engel M and Glotzer S C 2017 Shape and symmetry determine two-dimensional melting transitions of hard regular polygons *Phys. Rev.* X **7** 021001
[27] Butzhammer L, Völkel S, Rehberg I and Huang K 2015 Pattern formation in wet granular matter under vertical vibrations *Phys. Rev.* E **92** 012202
[28] Hough P V C 1962 Method and means for recognizing complex patterns *US Patent Specification* 3069654 inventor; United States Atomic Energy Commission, assignee
[29] Duda R O and Hart P E 1972 Use of the Hough transformation to detect lines and curves in pictures *Commun. ACM* **15** 11–5

[30] Kimme C, Ballard D and Sklansky J 1975 Finding circles by an array of accumulators *Commun. ACM* **18** 120–2

[31] Hollitt C 2012 A convolution approach to the circle Hough transform for arbitrary radius *Mach. Vis. Appl.* **24** 683–94

[32] Canny J 1986 A computational approach to edge detection *IEEE Trans. Pattern Anal. Mach. Intell.* **8** 679–98

[33] Ramming P and Huang K 2017 Clustering and melting in a wet granular monolayer *EPJ Web Conf.* **140** 08003

[34] Goyal S, Papadopoulos J M and Sullivan P A 1998 The dynamics of clattering: I. Equation of motion and examples *J. Dyn. Syst.* **120** 83

[35] Botev Z I, Grotowski J F and Kroese D P 2010 Kernel density estimation via diffusion *Ann. Stat.* **38** 2916–57

[36] McDonald A J and McDonald K T 2000 The rolling motion of a disk on a horizontal plane arXiv:physics/0008227

[37] Kessler P and O'Reilly O M 2002 The ringing of Euler's disk *Reg. Chaot. Dyn.* **7** 49–60

[38] Ma D, Liu C, Zhao Z and Zhang H 2014 Rolling friction and energy dissipation in a spinning disc *Proc. R. Soc.* A **470** 20140191

[39] Morin D 2008 *Introduction to Classical Mechanics* (Cambridge: Cambridge University Press)

[40] Shmilovitz D 2005 On the definition of total harmonic distortion and its effect on measurement interpretation *IEEE Trans. Power Deliv.* **20** 526–8

[41] Harth K, Kornek U, Trittel T, Strachauer U, Höme S and Will K 2013 Granular gases of rod-shaped grains in microgravity *Phys. Rev. Lett.* **110** 144102

[42] Abramson I S 1982 On bandwidth variation in kernel estimates-a square root law *Ann. Stat.* **10** 1217–23

[43] Silverman B W 1986 *Density Estimation for Statistics and Data Analysis* 1st edn (London: Taylor and Francis)

[44] Duin R P W 1976 On the choice of smoothing parameters for parzen estimators of probability density functions *IEEE Trans. Comput.* **25** 1175–9

[45] Agarwal N and Aluru N R 2010 A data-driven stochastic collocation approach for uncertainty quantification in MEMS *Int. J. Numer. Methods Eng.* **83** 575–97